NASA Technical Memorandum 4627

Measurement Uncertainty and Feasibility Study of a Flush Airdata System for a Hypersonic Flight Experiment

Stephen A. Whitmore and Timothy R. Moes

June 1994

NASA Technical Memorandum 4627

Measurement Uncertainty and Feasibility Study of a Flush Airdata System for a Hypersonic Flight Experiment

Stephen A. Whitmore and Timothy R. Moes
Dryden Flight Research Center
Edwards, California

MEASUREMENT UNCERTAINTY AND FEASIBILITY STUDY OF A FLUSH AIRDATA SYSTEM FOR A HYPERSONIC FLIGHT EXPERIMENT

Stephen A. Whitmore[*] and Timothy R. Moes[†]

NASA Dryden Flight Research Center, P. O. Box 273, Edwards, California 93523-0273

Abstract

Presented is a feasibility and error analysis for a hypersonic flush airdata system on a hypersonic flight experiment (HYFLITE). HYFLITE heating loads make intrusive airdata measurement impractical. Although this analysis is specifically for the HYFLITE vehicle and trajectory, the problems analyzed are generally applicable to hypersonic vehicles. A layout of the flush-port matrix is shown. Surface pressures are related airdata parameters using a simple aerodynamic model. The model is linearized using small perturbations and inverted using nonlinear least-squares. Effects of various error sources on the overall uncertainty are evaluated using an error simulation. Error sources modeled include boundary-layer/viscous interactions, pneumatic lag, thermal transpiration in the sensor pressure tubing, misalignment in the matrix layout, thermal warping of the vehicle nose, sampling resolution, and transducer error. Using simulated pressure data for input to the estimation algorithm, effects caused by various error sources are analyzed by comparing estimator outputs with the original trajectory. To obtain ensemble averages the simulation is run repeatedly and output statistics are compiled. Output errors resulting from the various error sources are presented as a function of Mach number. Final uncertainties with all modeled error sources included are presented as a function of Mach number.

Nomenclature

Acronyms and Initialisms

FADS	flush airdata sensing
HY-FADS	hypersonic flush airdata sensing
HYFLITE	hypersonic flight experiment
ICBM	intercontinental ballistic missile
MOS	model output statistic
NASP	National Aerospace Plane

Symbols

a	Knudsen's empirical constant (24.6)
A_c	tube cross-section areas, in^2
b	Knudsen's empirical constant (2.46)
c	sonic velocity, ft/sec; *also* Knudsen's empirical constant (3.15)
$C_{P_{max}}$	stagnation point pressure coefficient
C_{P_θ}	pressure coefficient at incidence angle
D	tube diameter, in.
D_{port}	port diameter, in.
F	aerodynamic model function
$g(M)$	Mach number function
$h(M)$	Mach number function
Int[...]	integer roundoff of real value
K	empirical coefficient for port damping (0.50)
L	tube length, in.
L_i	surface length, in.
L_{eff}	effective tubing length, in. (includes port effects)
M_∞	free-stream Mach number
M_2	downstream Mach number
P	pressure, lb/ft^2
$\hat{P}$	sampled pressure value, lb/ft^2
P_θ	pressure at incidence angle, θ, lb/ft^2
P_{02}	stagnation pressure downstream of shock, lb/ft^2
P_∞	free-stream static pressure, lb/ft^2
P_L	pressure at transducer, lb/ft^2

*Aerospace Engineer. AIAA member.
†Aerospace Engineer. AIAA member.

P_0	pressure at port, lb/ft²
$\bar{q}_\infty$	free-stream incompressible dynamic pressure, lb/ft²
q_2	dynamic pressure downstream of shock, lb/ft²
R	acoustic impedance (lbf-sec/ft³)
R_e	Reynolds number at surface
s	Laplace variable (1/sec)
t	skin thickness, in.
T_{avg}	average temperature in tube, °R (°F)
T_e	temperature at outer edge of boundary layer, °R (°F)
T_{surf}	surface temperature, °R (°F)
T_{trans}	transducer temperature, °R (°F)
T_w	adiabatic wall temperature, °R (°F)
$\vee$	transducer volume, in³
$V_{n,1}$	upstream velocity normal to shock wave, ft/sec
$V_{n,2}$	downstream velocity normal to shock wave, ft/sec
V_2	downstream velocity, ft/sec
V_∞	upstream velocity, ft/sec
X	longitudinal coordinate, in.
Y	lateral coordinate, in.
Z	normal coordinate, in.
α	angle of attack, deg
α_c	thermal expansion coefficient, carbon, in./in./°R
α_s	thermal expansion coefficient, steel, in./in./°R
β	angle of sideslip, deg
δ	ramp angle, deg
δ_{Hp}	pressure altitude residual, ft
δ_{M_∞}	free-stream Mach number residual, ft
δ_{p_∞}	free-stream pressure residual, ft
δ_{q_∞}	free-stream dynamic pressure residual, ft
δ_{Ri}	incremental radius of curvature resulting

	from heating, in.
δ_{Si}	incremental length change resulting from heating, in.
δ_α	angle-of-attack residual, deg
δ_β	angle-of-sideslip residual, deg
δ_θ	incidence angle residual, deg
ϕ	clock angle, deg
γ	ratio of specific heats
Γ	oblique shock angle, deg
η	white noise source
κ	Knudsen number
λ	cone angle, deg
μ	dynamic viscosity, lbf-sec/ft
θ	incidence angle, deg
ρ	density, lbm/ft³
σ	standard deviation
ξ	damping ratio
$\bar{\chi}$	viscous interaction parameter
ω_n	natural frequency, rad/sec
∇	gradient of vector

Subscripts

i	port index
j	iteration index
∞	free-stream parameter
0	initial condition of parameter
2	parameter downstream of shock

Introduction

The former National Aerospace Plane (NASP) program proposed a hypersonic flight experiment (HYFLITE) to evaluate the performance of scramjet technologies.[1] The proposed vehicle has a forebody shape resembling the NASP, and was designed to support a scramjet test engine. This paper presents the results of a feasibility study and error analysis performed for a hypersonic flush airdata system (HY-FADS) on the HYFLITE vehicle. The study and analyses are based on models generally accepted as valid within the aerospace community. Some parts of the system are not modeled and are so noted. Although the analysis

performed is specific to the HYFLITE vehicle and trajectory, the methods described and the problems analyzed are generally applicable to other hypersonic vehicles. This paper addresses feasibility and accuracy issues common to most hypersonic vehicles.

This study presents the physical layout of a candidate flush-port matrix, and the effects of various error sources on the overall system uncertainty are evaluated using an error simulation. In this simulation a realistic set of pressure data is generated along the trajectory, and various error sources are superimposed on the data. Using the simulated pressure data (with the various error sources superimposed) for input to the airdata estimation algorithm, estimates of the trajectory parameters are generated. The effects caused by the various error sources are analyzed by comparing the outputs of the estimation algorithm with the original trajectory data. To obtain ensemble averages of the errors induced by random input error components, the simulation is run repeatedly and model output statistics (MOSs) are generated. Output error magnitudes resulting from the various (input) error sources are presented as a function of Mach number. The peak Mach number analyzed is approximately 13 and the peak altitude is 120,000 ft. This report analyzes only supersonic and hypersonic conditions.

Background

Because airdata values are used to normalize performance and flight mechanics parameters and to schedule control and guidance system gains or to provide direct flight control feedback, accurate airdata measurements have always been critical for the flight test community. Although the requirements for measurement uncertainty for hypersonic vehicles have been difficult to firmly establish, uncertainties for Mach number of about 0.10 and flow incidence angles of about 0.25° have frequently been requested. Accuracies on this level are needed for engine flowpath and vehicle trajectory optimization

Historically, airdata measurements were obtained using intrusive booms that extended beyond the local flow field of the aircraft and measured airmass velocities by directly stagnating the flow via a pitot tube at the end.[2] Flow incidence angles were measured using mechanical vanes attached to the probe. Because heating loads induced by hypersonic vehicles make it difficult for intrusive measurement devices to survive, probes are considered impractical for hypersonic vehicles.

To bypass the difficulties with intrusive systems, the flush airdata sensing (FADS) system concept, in which airdata are inferred from nonintrusive surface pressure measurements, was developed in the early 1960's and used to measure hypersonic conditions on the Saturn IVb space launch vehicle and X-15 rocket. The concept was further

refined during the shuttle reentry airdata sensing experiment, which demonstrated that the concept was feasible for blunt-nosed hypersonic vehicles. Concurrent with the shuttle experiment, early aeronautical applications included programs conducted at NASA Dryden Flight Research Center on the KC-135 and F-14 vehicles.[4,5] Later programs at NASA Dryden demonstrated the autonomous capability of the system, with fully redundant systems being demonstrated on the F-18 High Alpha Research Vehicle and autonomous real-time systems demonstrated on the F-18 Systems Research Aircraft.[6,7] References 8 and 9 provide an overview of failure detection and fault management techniques developed for the real-time FADS system.

The FADS method offers the advantage of inferring dynamic pressure, Mach number, and flow incidence angles without requiring that the stagnation flow condition be created and measured directly. This approach allows the heating load at the pressure orifices to be significantly diminished for orifices positioned away from the forebody stagnation point and makes the FADS method ideal for application to hypersonic vehicles.

Trajectory and Vehicle Description

HYFLITE achieves high Mach numbers at high dynamic pressures using a depressed trajectory. To reach this trajectory an intercontinental ballistic missile boosts a test article to hypersonic conditions suitable for performing scramjet research.[1] This trajectory accelerates the vehicle to approximately Mach 13 at 120,000 ft with peak dynamic pressures of 2800 lb/ft^2. Figure 1 shows the proposed flight envelope.
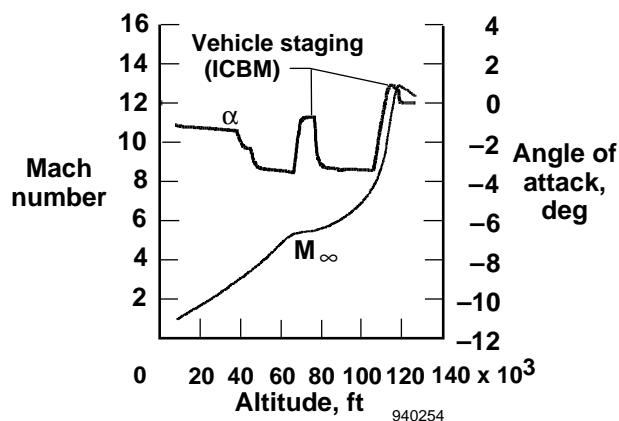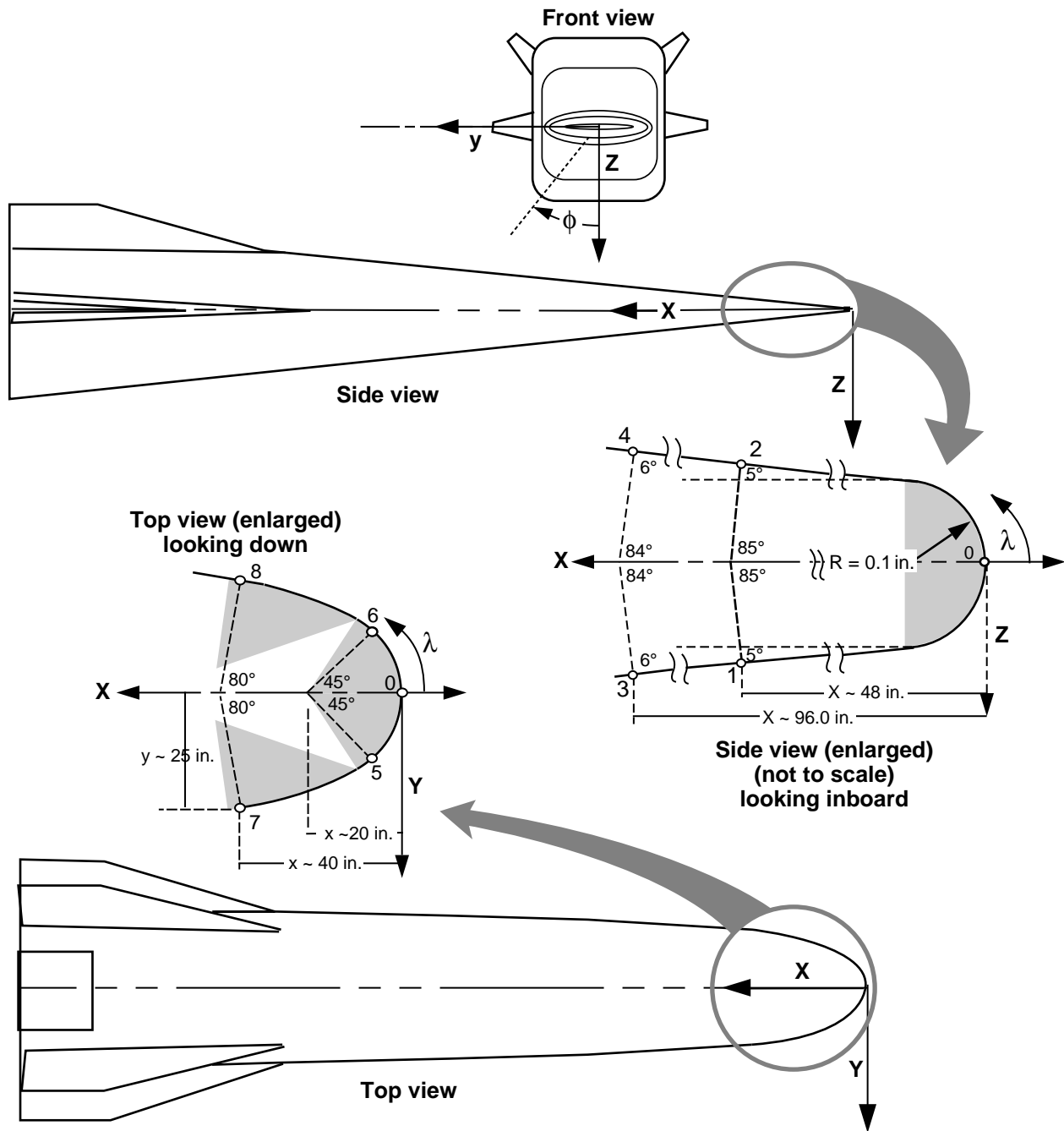

Fig. 1. HYFLITE vehicle flight envelope.

Figure 2 pictures the vehicle to be analyzed. The proposed configuration resembles the NASP forebody and was designed to support a scramjet test engine. The vehicle has a shovel-like nose with 5° wedge angles at the

Fig. 2. Proposed pressure FADS port locations for HYFLITE vehicle.

leading edge. The top surface ramp expands to a 6° half angle approximately halfway aft, and the lower surface has an isentropic compression ramp for the scramjet fixture. For this study the isentropic ramp was approximated by a 6° wedge. The longitudinal leading-edge radius of the nose is 0.1 in., and the lateral leading-edge radius is approximately 20 in. The approximate vehicle length is 33 ft. Although the leading edge—which was chosen to give good flow characteristics at the scramjet inlet for single-stage-to-orbit performance—is quite sharp, this

analysis assumes that the leading edge is blunt enough to allow sufficient heating relief for the nose to withstand the resulting surface temperatures without active cooling.

Airdata System Port Layout

The port matrix layout was determined as a compromise between the need to accurately model the flow characteristics near the pressure ports, and the need to give good sensitivity of the pressure measurements relative to the airdata

4

parameters. Regions where high-temperature viscous interactions cause boundary-layer thickening were avoided. Only locations along the leading edge (where the boundary-layer thickness is small) and locations farther aft on the ramp surfaces (where the viscous interactions diminish) were considered.

Results presented in references 6, 7, 8, and 9 show that more ports always lead to more accurate measurements, but that diminishing returns are reached when the number of ports exceeds nine. Below this number of ports, airdata measurement errors can rise significantly. Thus, a total of nine ports was used: five along the leading edge and four distributed on the centerline of the two-dimensional ramp surfaces. The ports along the leading edge provide the primary information source for measuring Mach number (M), angle of sideslip (β), and static pressure (pressure altitude, Hp). The ports on the upper and lower ramp surfaces provide the primary information source for angle-of-attack (α) measurement.

The port locations are described using a clock and cone angle coordinate system that is an analytical mapping from the actual surface to a hemisphere. The cone angle, λ, is the total angle that the normal to the surface makes with respect to vehicle axis of symmetry. The clock angle, ϕ, is the clockwise angle looking aft around the axis of symmetry starting at the bottom of the fuselage. As mentioned earlier, to keep the locations of the leading-edge ports far enough forward on the vehicle so that boundary-layer effects could be ignored, ports were placed near the nose with cone angles of 0°, ±45°, and ±80°. The ramp ports were placed farther aft on the vehicle where the effects of viscous interactions diminish. The first set of ports were located approximately 4-ft aft of the nose, and the second set 8 ft aft. Figure 2 depicts the HYFLITE vehicle and approximate port locations. Table 1 lists the coordinate angles of the pressure ports.

Table 1. Pressure port coordinates.

Port no.	λ, deg	ϕ, deg	Location
0	0	0	Stagnation
1	85	0	Lower ramp
2	85	180	Upper ramp
3	84	0	Lower ramp (aft)
4	84	180	Upper ramp (aft)
5	45	–90	Leading edge
6	45	90	Leading edge
7	80	–90	Leading edge (aft)
8	80	90	Leading edge (aft)

The angles of attack and sideslip, α and β, are related to the port coordinate angles[6] by

$$\cos(\theta_i) = \cos(\alpha)\cos(\beta)\cos(\lambda_i) +$$
$$\sin(\beta)\sin(\phi_i)\sin(\lambda_i) + \sin(\alpha)\cos(\beta)\cos(\phi_i)\sin(\lambda_i)$$

where θ_i is the total incidence angle relative to the local surface.

Pressure Modeling

The key to this analysis is to develop a pressure model that relates the airdata to the surface pressures in an accurate way, but is still simple enough to be inverted and implemented as part of an airdata estimation algorithm. For accuracy equilibrium high-temperature gas effects must be modeled in the analysis. Because Mach number peaks out in the Mach 12 region, however, previous results[10] indicate that nonequilibrium high-temperature gas effects are not significant, and they were ignored in this analysis. Because pressure is a mechanical quantity and depends primarily upon the mechanical aspects of the flow, influences caused by high-temperature gas chemistry are always secondary. Viscous boundary-layer interactions are significant, however; errors resulting from the interactions were modeled and their effects introduced in the error analysis section.

Near the leading edge the stagnation properties ($C_{P_{max}}$) were computed using the high-temperature equilibrium normal shock tables and equations of state for air,[11, 12] and the pressure distribution was described using modified Newtonian flow.[10]

$$\frac{P_\theta - P_\infty}{\bar{q}_\infty} = C_{P_\theta} = \frac{P_{02} - P_\infty}{\bar{q}_\infty}\cos^2(\theta) =$$
$$C_{P_{max}}\cos^2(\theta) \tag{1a}$$

On the ramp surfaces, the pressure distribution was computed using the equilibrium normal shock tables and the shock wave angle–turning angle relationship for high-temperature equilibrium flow.[10] Here, the oblique shock angle, Γ, is an implicit function of the free-stream velocity and the surface wedge (turning) angle, δ

$$\tan(\Gamma - \delta) = \frac{V_{n,2}}{V_{n,1}}\tan(\Gamma) \tag{1b}$$

where $V_{n,1}$ is the upstream velocity normal to the shock wave, and $V_{n,2}$ is the downstream velocity normal to the shock wave. The ratio

$$\frac{V_{n,2}}{V_{n,1}} = \frac{V_2 \sin(\Gamma)}{V_\infty \sin(\Gamma)}$$

is determined from the equilibrium normal shock tables. For a given turning angle, equation (1b) is iterated until the velocity ratio is consistent with the normal shock tables. Once the shock angle and downstream velocity have been determined, the downstream pressure coefficient is determined from the equations of continuity and momentum,[13]

$$\rho_2 V_2 = \rho_1 V_1,$$

$$P_2 + \rho_2 [V_2 \sin\Gamma]^2 = P_1 + \rho_1 [V_2 \sin\Gamma]^2$$

to give

$$Cp_{wedge} = 2\sin^2[\Gamma]\left[1 - \frac{V_2}{V_1}\right] \tag{1c}$$

The clock angle is always either 180° for the upper surface ramp or 0° for the lower surface ramp; thus, the incidence angle is related to the wedge half-angle by

Upper Surface:
$$\cos(\theta_i) = [\cos(\alpha)\sin(\delta) - \sin(\alpha)\cos(\delta)]\cos(\beta)$$

Lower Surface:
$$\cos(\theta_i) = [\cos(\alpha)\sin(\delta) + \sin(\alpha)\cos(\delta)]\cos(\beta)$$

Equations (1a), (1b), and (1c), along with the high-temperature equilibrium normal shock tables for air, can be used to simulate pressure data along the vehicle flight trajectory. This system of equations was also used as the model that relates the measured pressure to the airdata states in the airdata estimation algorithm.

Airdata Estimation Algorithm

This section develops the regression algorithm that was used to extract the airdata estimates from the pressure data. For this analysis the *airdata state vector* is described in terms of four parameters: dynamic pressure behind the shock (q_2), angle of attack (α), angle of sideslip (β), and free-stream static pressure (P_∞). Using these four basic airdata parameters, other airdata quantities of interest may be directly calculated. For a given pressure observation the form of the model is

$$P(\phi_i, \lambda_i) = F\left(\begin{bmatrix} q_2 \\ P_\infty \\ \alpha \\ \beta \end{bmatrix}, \phi_i, \lambda_i, \gamma, M_\infty\right) + \eta_i \tag{2a}$$

The specific form of the nonlinear function $F[\ldots]$ depends on whether the port is located on the leading edge or on the ramp surfaces. The parameter η_i is a noise vector and can be used to represent the various modeling-, system-, and measurement-error sources. Taken together, the matrix of ports forms an overdetermined nonlinear model in that the number of observations (9) is larger than the number of states to be estimated (4).

The system is nonlinear in α and β, and Mach number is a parameter of the system, which is in turn related to the airdata parameters. As a result of this nonlinearity and interdependence, the system of equations must be solved iteratively to estimate the airdata states. This iteration is implemented by linearizing about a starting value for each port, and the perturbations between the measured (generated) data and the model predictions are evaluated. At a given data frame for each pressure port, $i = 1, \ldots N$,

$$\delta P_i^{j+1} = [P_i - F^j(\alpha, \beta, q_2, P_\infty, \lambda_i, \phi_i, M_\infty)] =$$

$$\nabla_{\begin{bmatrix} q_2 \\ P_\infty \\ \alpha \\ \beta \end{bmatrix}} F_i^j \times \begin{bmatrix} \delta P_2^{j+1} \\ \delta P_\infty^{j+1} \\ \delta \alpha^{j+1} \\ \delta \beta^{j+1} \end{bmatrix} + \ldots \tag{2b}$$

Defining

$$\begin{bmatrix} q_2^{j+1} \\ P_\infty^{j+1} \\ \alpha^{j+1} \\ \beta^{j+1} \end{bmatrix} = \begin{bmatrix} q_2^{j} \\ P_\infty^{j} \\ \alpha^{j} \\ \beta^{j} \end{bmatrix} + \begin{bmatrix} \delta q_2^{j+1} \\ \delta P_\infty^{j+1} \\ \delta \alpha^{j+1} \\ \delta \beta^{j+1} \end{bmatrix}$$

the updated state vector is solved using recursive least squares

$$\begin{bmatrix} q_2^{j+1} \\ P_\infty^{j+1} \\ \alpha^{j+1} \\ \beta^{j+1} \end{bmatrix} = \begin{bmatrix} q_2^{j} \\ P_\infty^{j} \\ \alpha^{j} \\ \beta^{j} \end{bmatrix} + \left[(\nabla^T F)(\nabla F)\right]^{-1}(\nabla^T F) \begin{bmatrix} \delta P_1^{j+1} \\ \vdots \\ \delta P_N^{j+1} \end{bmatrix} \tag{2c}$$

At the end of each iteration cycle the downstream Mach number, M_2, is determined from the ratio of q_2/P_∞. P_∞ is used to determine the altitude, and the temperature is determined using a standard atmosphere. With these values for pressure, temperature, and M_2, free-stream Mach

number is determined using a table lookup of the equilibrium normal shock tables for air. For each data frame the iteration cycle is repeated until algorithm convergence is reached—typically from 2 to 5 cycles. For this algorithm free-stream Mach number is used as the convergence criterion, and changes in the free-stream Mach number of less than 0.001 are considered to indicate a converged cycle. At the beginning of each new data frame, the system of equations is linearized about the result of the previous data frame. The Choleski factorization techniques used to perform the regression are standard imple-mentations[14] and will not be discussed here.

Error Analysis: Development of Error Models

In this section error sources for the pressure measurements are considered, and error propagation models, both random and systematic, are developed. These error models are used to contaminate the pressure data. The corrupted pressure data are subsequently used as input to the airdata estimation algorithm. The simulation is designed to allow errors to be superimposed individually or in groups. Imposition of the errors individually allows the magnitudes of the various effects to be quantified individually.

This error analysis assumes that the flow models described earlier are accurate. Except those made for viscous boundary-layer interaction, no attempt is made to characterize the uncertainty of the surface pressure models. The error models developed address only the local measurement error sources. Vehicle dependent effects, such as bending about the center of gravity and position error,[2] are not considered. For a real vehicle, these effects must be calibrated.

Viscous Interaction Error Model

As mentioned previously, equilibrium high-temperature gas effects are included in the estimation model, and non-equilibrium high-temperature effects are considered negligible in this analysis. Because the shock is detached near the nose, shock-boundary-layer interactions can be ignored. At high free-stream velocities, however, viscous interactions between the boundary layer and the external flow can significantly increase the boundary-layer thickness, which can in turn significantly affect the local pressure distribution. Based on the analysis of reference 10, the induced pressure error (caused by viscous interactions) is directly proportional to the governing similarity parameter, $\bar{\chi}$, where

$$\bar{\chi} = \frac{M_\infty^3}{\sqrt{R_e}} \sqrt{\frac{\rho_w \mu_w}{\rho_e \mu_e}} = \frac{M_\infty^3}{\sqrt{R_e}} \sqrt{\frac{\frac{P_w}{RT_w}\mu_w}{\frac{P_e}{RT_e}\mu_e}} \tag{3a}$$

The subscript w indicates quantities at the wall, and the subscript e represents quantities at the outer edge of the boundary layer. If pressure is constant (vertically) throughout the boundary layer and viscosity is proportional to the square root of the temperature,[11] then

$$\bar{\chi} = \frac{M_\infty^3}{\sqrt{R_e}} \sqrt{\frac{T_e \mu_w}{T_w \mu_e}} \approx \frac{M_\infty^3}{\sqrt{R_e}} \left[\frac{T_e}{T_w}\right]^{1/4} \tag{3b}$$

Assuming an adiabatic wall (with a recovery factor of Rc),

$$\bar{\chi} \approx \frac{M_\infty^3}{\sqrt{R_e}\left[1 + \frac{Rc(\gamma-1)}{2}M_\infty^2\right]^{1/4}} \tag{3c}$$

A value of $\bar{\chi} < 3$ indicates a weak boundary-layer interaction, and a value of $\bar{\chi} \geq 3$ indicates a strong interaction. For a flat plate the increment in pressure resulting from a weak interaction is approximately[10]

$$\left[\frac{\delta P_{viscous}}{P_{inviscid}}\right]_{weak} \approx 1 + 0.31\bar{\chi} + 0.05\bar{\chi}^2 \tag{4a}$$

and the increment in pressure resulting from a strong interaction is approximately

$$\left[\frac{\delta P_{viscous}}{P_{inviscid}}\right]_{strong} \approx 0.514\bar{\chi} - 0.241 \tag{4b}$$

If the wall is nonadiabatic such as for an actively cooled surface, then the viscous interaction errors will be less than those predicted by equations (3) and (4). Thus, the viscous interaction analysis is conservative.

Pneumatic Lag Error Model

Because of the hostility of the surface environment, surface pressures must be sensed by transducers located remotely within the aircraft body. The measurement transducers are connected to the surface via lengths of pneumatic tubing. This tubing induces spectral distortion caused by frictional losses and wave resonance. Based on the analysis described in reference 7, the pneumatic attenuation effects are modeled by a time-varying, second-order system of the form

$$\frac{P_L(S)}{P_0(S)} = \frac{1}{\frac{1}{\omega_n^2}s^2 + 2\frac{\xi}{\omega_n}s + 1} \tag{5a}$$

7

where P_L is the pressure measured at the transducer and P_0 is the surface pressure input. The natural frequency of the system is described by

$$\omega_{n^2} = \frac{\dfrac{(A_c c^2)}{LV}}{\left\{\left(\dfrac{LA_c}{2V_e}\right)\left[1 + \dfrac{(LR)^2}{12(\rho_0 c)^2}\right] + \left[1 + \dfrac{(LR)^2}{6(\rho_0 c)^2}\right]\right\}}$$

and the damping ratio is given by

$$\xi = \frac{R\omega_n}{2\rho_0}\left[\frac{L^2}{2c^2} + \frac{LV}{A_c c^2}\right]$$

where L is the tubing length, A_c is the tube cross-sectional area, c is the local sonic velocity, ρ_0 is the local density (within the tube), and V is the entrapped volume of the transducer. Assuming laminar flow in the tube the acoustic impedance of the system is defined by

$$R = \frac{32\mu}{D^2}$$

For each pressure sensor ξ and ω_n are evaluated at each time point based on an average of the surface conditions and the conditions at the transducer.

The effects of the surface pressure ports are modeled using the analyses of references 16 and 17. Here the effect of the port is to extend the effective length of the tube by the amount

$$\delta L_{eff} = \frac{8D_{port}}{3\pi} + \frac{KD_{port}}{64}Rey \qquad (5b)$$

where γ, P, M, μ, and c are evaluated based on local conditions, and D_{port} is the port diameter. Entrapped volumes found where the tube joins the surface port are ignored. For this analysis the effective increment in tubing length is small, about 1 to 5 percent of the total length.

Thermal Transpiration Error Model

The transpiration-induced pressure nonequilibrium, which results from large temperature gradients and small tubing diameters, is primarily a molecular flow phenomenon.[18] Along an unequally heated gas boundary, kinetic theory predicts that the gas adjacent to the boundary wall will creep from the colder region to the hotter region. For static conditions in which there is no net mass flow within the tube, to balance this creep the gas in the center of the tube tends toward the colder end of the tube. The result of

this opposing flow is that a static pressure gradient is established, with the cold region of the tube reading lower than the hot region. This effect, referred to as transpiration or molecular creep, is primarily a steady-state phenomenon.

For high ambient pressure levels at which continuum flow exists, the molecular creep effect is not considered important and can be ignored. At low-pressure levels, however, this effect becomes important. For low-pressure conditions the pressure gradient induced by longitudinal temperature gradients is primarily a function of Knudsen's number, κ. If the characteristic length of the system is taken to be the tube diameter, then for air

$$\kappa \approx \left[51.9\frac{ft}{\sec\sqrt{°R}}\right]\frac{\mu}{D}\frac{\sqrt{T}}{P}$$

The transpiration effect is modeled by numerical integration of Knudsen's molecular creep equation[18]

$$\frac{\partial P(x)}{\partial T(x)} =$$
$$\frac{1}{2}\frac{P(x)}{T(x)}\left[\frac{\kappa(p, T, D)(\kappa(p, T, D) + a)}{\kappa(P, T, D)^2 + (a + b)\kappa(P, T, D) + bc}\right]^2$$

$$(6)$$

where the constants a, b, and c have been empirically determined to be

	$\underline{a}$	$\underline{b}$	$\underline{c}$
Knudsen's constants	24.6	2.46	3.15

and D is the tube diameter. For a prescribed value of D equation (6) may be treated as an initial value problem, which is integrated over a prescribed temperature range from the transducer to the surface. It can then be implemented as a part of the overall simulation scheme.

Port Misalignment Error Models

This analysis models the effects of port alignment errors. Two types of errors are modeled: (1) an initial (random) error in the port alignment and (2) systematic deformation of the structure resulting from heating loads.

Initial Port Misalignment Error Model

The clock and cone angle bias alignment errors were introduced into the simulation at the beginning of each Monte-Carlo time history run using a normalized random-number generator. Once the values of the alignment errors have been set for a particular data run, they are held constant throughout the data run.

Structural Deformation Error Model

Modeling of the thermal expansion of the highly curved leading edge is extremely difficult, and only the deformation of the ramp surfaces is addressed in this model. The analysis is for a flat plate with the primary deformation mechanism assumed to be differential expansion of the skin layers. Referring to figure 3, the skin is assumed to be carbon-carbon on the exterior bonded to a stainless steel substrate on the interior. The thermal expansion coefficients are α_c (carbon-carbon) and α_s (stainless steel). Assuming identical thickness for the two layers, then based on the analysis of reference 16, the radius of curvature resulting from differential thermal expansion of the two layers is

$$\delta_{Ri} = \frac{2t}{3(\alpha_c - \alpha_s)(T_i - T_{ref})} \tag{7a}$$

where δ_{Ri} is the induced radius of curvature at the ith port, t is the thickness of the skin (carbon-carbon and stainless steel), T_i is the temperature at the surface, and T_{ref} is the reference temperature at which the skins were bonded. Referring to figure 3, the differential incidence angle is given by

$$\delta_{\theta i} = \frac{\delta_{Si}}{\delta_{Ri}} \tag{7b}$$

where δ_{Si} is the length expansion to the surface. From reference 17 the expansion per unit length is given by

$$\frac{\delta_{Si}}{L_i} = \frac{\alpha_c}{2}(T_i - T_{ref}) \tag{7c}$$

and the resulting deformation model is then given by

$$\delta_{\theta i} = \frac{3}{4}\frac{L_i}{t}((\alpha_c)^2 - \alpha_c\alpha_s)(T_i - T_{ref})^2 \tag{7d}$$
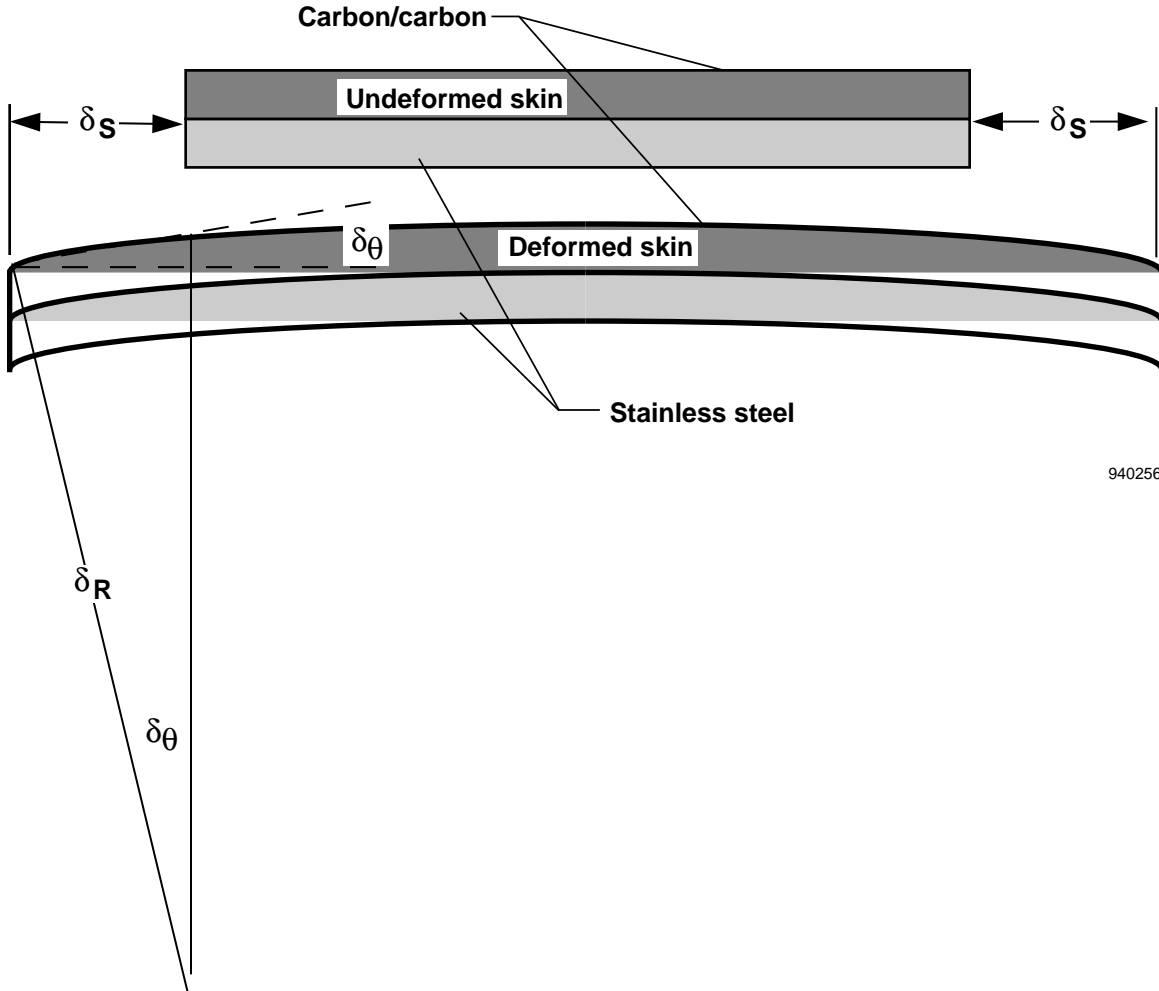
Fig. 3. Thermal expansion deformation model for HYFLITE skin.

9

For this analysis the per-length parameter, L_i, is the distance over which the heating has occurred and for this analysis is defined as the distance from the tip of the vehicle to the port.

Resolution and Transduction Error Models

System quantization levels of 12 and 16 bits are analyzed. To simulate this quantization the generated pressure data are sampled and truncated after n bits (2^n counts) of resolution.

$$\hat{P}_i = \text{Int}\left[\frac{P_i}{Full\ Scale\ Reading} \times 2^n\right] \times \frac{Full\ Scale\ Reading}{2^n}$$

$$(8)$$

This analysis assumes that the measurement transducers are located in an environmentally controlled area, and that the manufacturer's environmental specifications are not exceeded. Furthermore, it is assumed that known bias errors are eliminated using preflight tare calibrations; unknown bias errors or variable but systematic transduction errors are lumped with the random errors for this analysis. The random transducer errors are modeled as unbiased Gaussian white noise sequences and are generated using a normalized random-number generator. The errors are allowed to vary randomly for each data frame and across the collection of pressure ports.

Results and Discussion

The results of the error analysis will now be presented. Figures 4 through 10 show sample residuals (from one of the Monte-Carlo data runs) for each of the error sources. For the final uncertainty analysis of the system, all error sources are superimposed simultaneously. The model outputs from 100 data runs are averaged to give ensemble statistics. Table 2 lists root-mean-square (1-σ rms) error statistics.
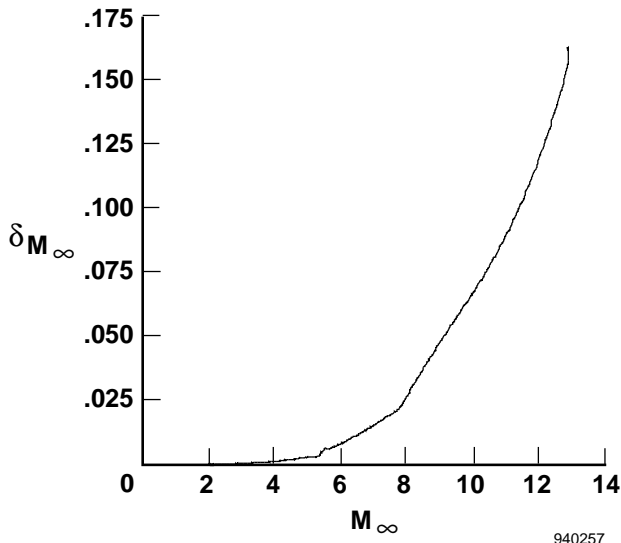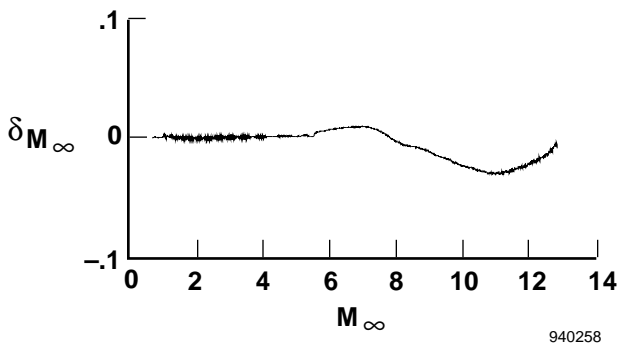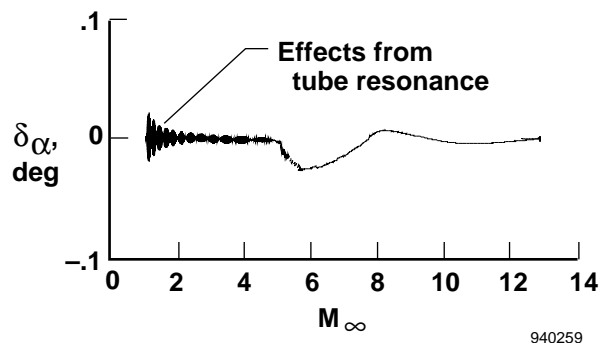

Fig. 4. Mach-number residual caused by high-temperature viscous-boundary-layer interactions.
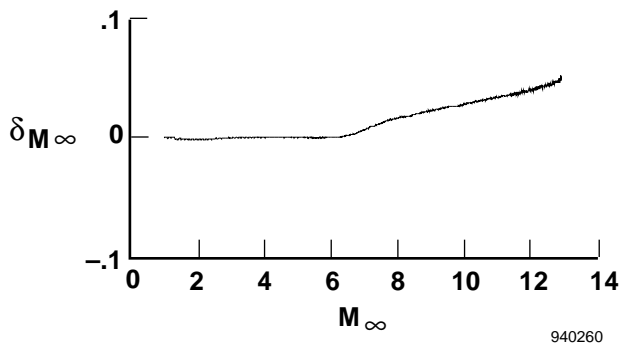

(a) Mach-number residual.

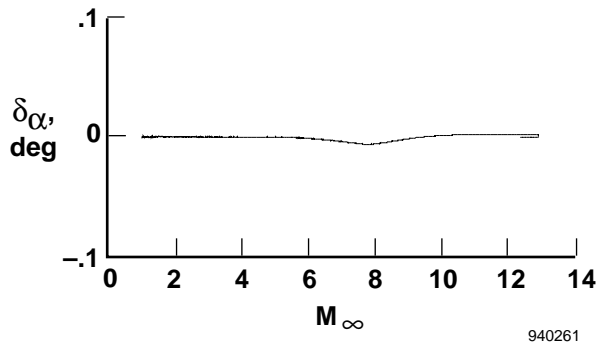Fig. 5. Residuals caused by pressure-tubing lags, resonances, and attenuations.

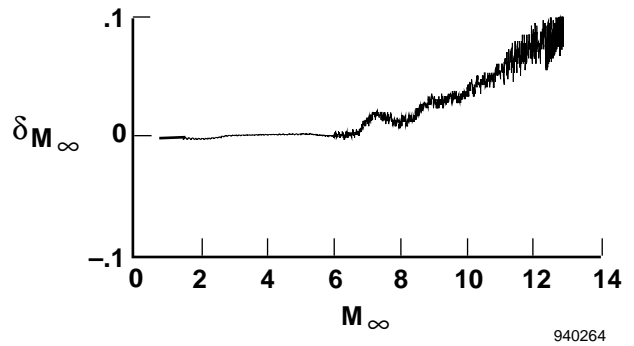(b) Angle-of-attack residual.

Fig. 5. Concluded.

(a) Mach-number residual.

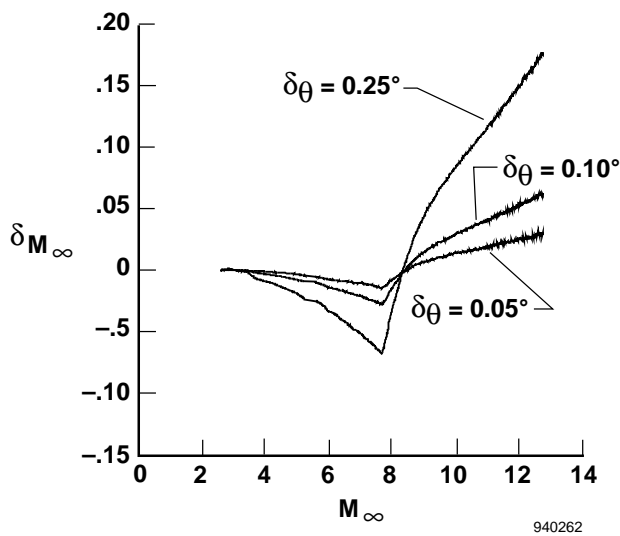Fig. 6. Residuals caused by thermal transpiration of pressure tubes.
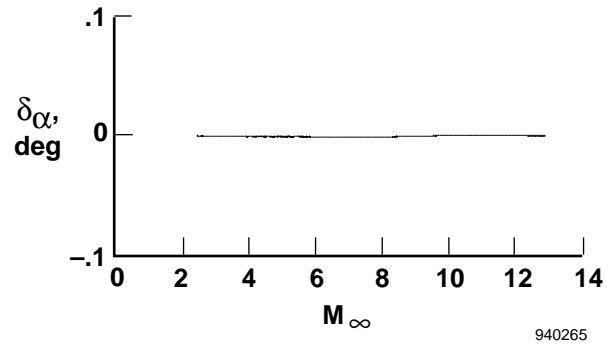
10

(b) Angle-of-attack residual.

Fig. 6. Concluded.

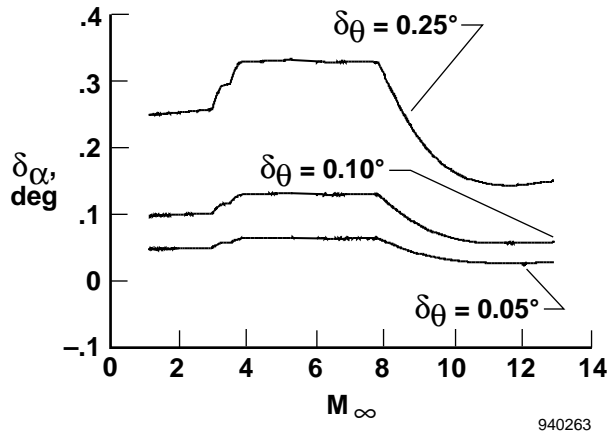**(a) Mach-number residual.**
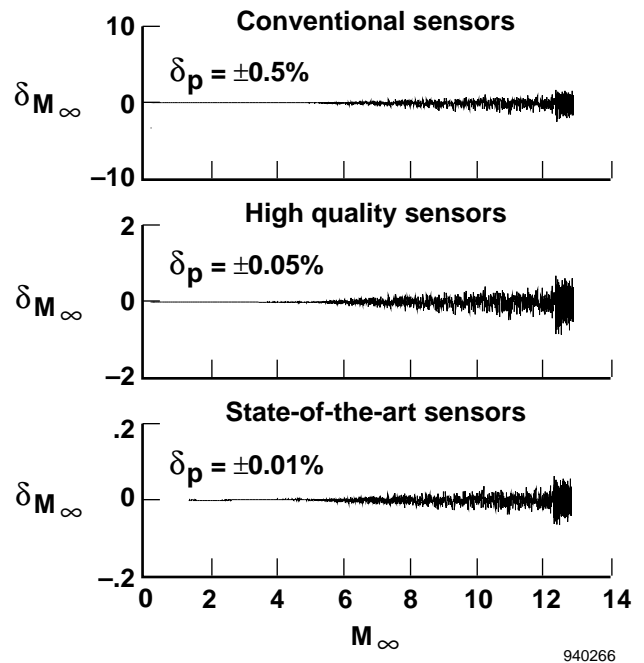

(a) Mach-number residual.

(b) Angle-of-attack residual.

Fig. 8. Residuals caused by heating-induced structural deformation.
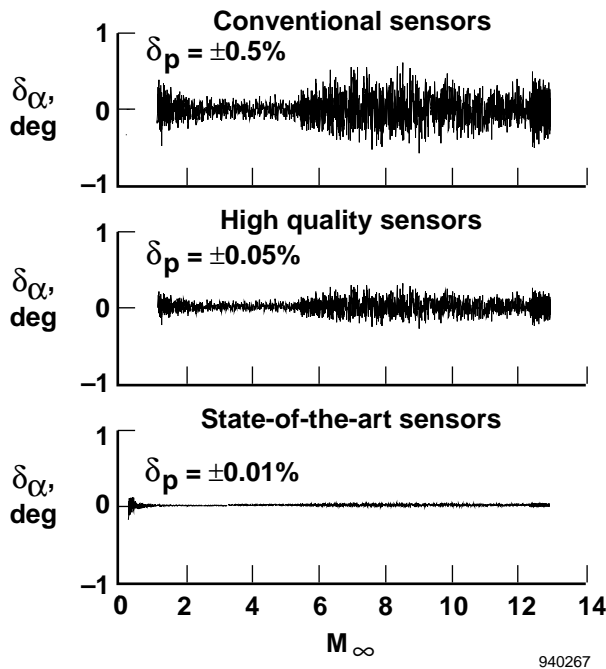

(b) Angle-of-attack residual.
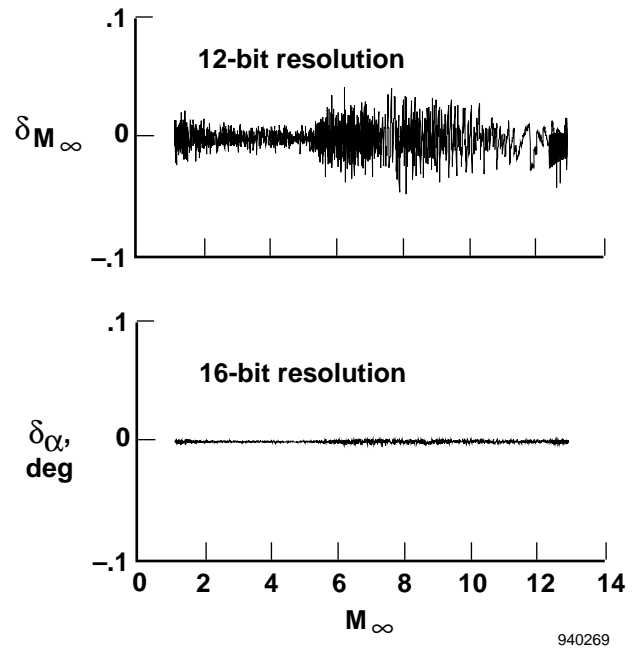
Fig. 7. Residuals caused by initial port misalignment error.

(a) Mach-number residuals.

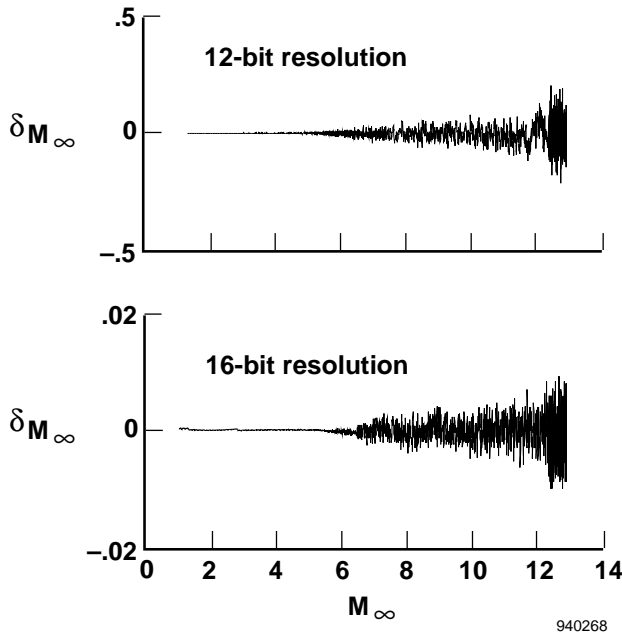**Fig. 9. Residuals caused by transducer error.**

11

(b) Angle-of-attack residuals.

Fig. 9. Concluded.

(b) Angle-of-attack residuals.

Fig. 10. Concluded.

(a) Mach-number residuals.

Fig. 10. Residuals caused by measurement system resolution error.

Errors Caused by Viscous Interactions

In this analysis the data were simulated using the analysis of equations (3) and (4) to superimpose viscous interaction pressure errors onto the baseline data. Because the analysis of equations (3) and (4) is invalid near the leading edge, errors introduced by boundary-layer interactions were modeled only for the ramp ports and the $80°$ pressure ports. The estimation algorithm was run, and the resulting trajectory was compared with the original trajectory. The Mach-number residuals between the estimated airdata and the actual trajectory were computed, and figure 4 shows these results. The effect on Mach number is significant only beyond Mach 8, with a peak error of 0.17 (at Mach 12.5). Because the upper and lower ramp pressures are affected equally by the viscous interactions, little influence is experienced by the angle-of-attack measurements.

Errors Caused by Pneumatic Lag and Attenuation

In this section the errors induced by the pneumatic arrangement of the airdata system are analyzed. Because the damping ratio and the time lag of the pressure measurement sensors vary inversely with the mean density level in the tube, the responses of the ports near the stagnation point are much less damped. In addition the lags for these ports are significantly shorter than those for the ports located away from the stagnation point where the pressure and density levels are lower. Because the HY-FADS algorithm is time independent, this mixture of time delays and damping manifests itself as a data distortion that becomes

Table 2. 1-σ rms absolute and 1-σ rms percentage error estimates for the HY-FADS system.

M_∞	δ_{M_∞}	$\delta_{\bar{q}}$, lb/ft^2	δ_{Hp}, ft	δ_α, deg	δ_β, deg	$\delta_{M/M}$, %	$\delta_{\bar{q}/\bar{q}}$, %	$\delta_{Hp/Hp}$, %
1.0	0.0	1.0	10	0.2	0.1	0.3	0.1	0.1
2.0	0.0	1.5	10	0.2	0.2	0.2	0.1	0.0
3.0	0.0	0.3	10	0.1	0.2	0.1	0.0	0.0
4.0	0.0	0.8	25	0.1	0.2	0.1	0.0	0.1
5.0	0.0	4.0	100	0.2	0.3	0.2	0.2	0.2
6.0	0.0	5.0	250	0.2	0.3	0.4	0.6	0.2
7.0	0.0	2.0	350	0.2	0.3	0.6	0.3	0.3
8.0	0.1	1.0	450	0.2	0.4	1.0	0.1	0.4
9.0	0.1	3.0	500	0.2	0.3	1.1	0.4	0.5
10.0	0.1	3.0	600	0.2	0.3	1.2	0.3	0.5
11.0	0.2	2.0	750	0.2	0.3	1.6	0.2	0.7
12.0	0.3	1.0	1100	0.2	0.3	2.3	0.1	0.8
12.5	0.4	4.0	1350	0.2	0.3	3.3	0.4	1.0

most pronounced at high Mach numbers, at which the spread of damping and lags is greatest. Thus, it is generally a good idea to match the lags and damping of the various sensors as closely as possible over the range of test conditions. A practical system with minimal pneumatic effects (except an inherent time-latency) can generally be achieved by varying the lengths and diameters of the connective tubing. Table 3 lists the configuration used for this simulation.

Table 3. Pneumatic layout of airdata system.

Port no.	λ, deg	ϕ, deg	Tube diameter, in.	Tube length, in.	Port diameter, in.
0	0	0	0.020	60	0.010
1	85	0	0.060	24	0.020
2	85	180	0.060	24	0.020
3	84	0	0.060	24	0.020
4	84	180	0.060	24	0.020
5	45	−90	0.020	60	0.010
6	45	90	0.020	60	0.010
7	80	−90	0.060	24	0.020
8	80	90	0.060	24	0.020

For this analysis it is assumed that the transducers are located in a thermally controlled environment and that the transducer temperature is maintained at 100 °F for the duration of the flight. The volume entrapped by the transducer is assumed to be minimal, and a value of 0.05 in^3 was used. To eliminate problems with surface heating, the external port size is constrained to be 0.01 in. for all leading-edge ports and 0.02 in. for the ramp surface ports. The model parameters are computed using the average of the surface and transducer temperatures. Temperatures at the external ports are computed using the equilibrium oblique shock equations for the ramp ports, and the equilibrium normal shock tables for the leading-edge ports. The gas density within the pressure tubes was evaluated using the input pressure level and the average between the surface temperature (computed from equilibrium analysis) and the assumed transducer temperature (100 °F). Figure 5(a) shows the resulting Mach number residuals, and the angle-of-attack residuals are shown in figure 5(b).

Errors Caused by Thermal Transpiration

The thermal transpiration or molecular creep error analysis was performed using the configuration analyzed in the previous section. Figure 6 presents Mach-number and angle-of-attack residuals. Again the effect on Mach number is significant only beyond Mach 6. It is at these speeds where the conditions rarefied enough to induce molecular effects. The effects on angle of attack are insignificant.

13

Errors Caused by Port Misalignment

This section presents the results of the port misalignment error analyses. Errors resulting from the initial port misalignment will be presented first. The errors resulting from systematic deformation of the structure caused by heating loads will be presented next.

Initial Port Misalignment Error

For this analysis the three initial misalignment error bounds were considered—0.05°, 0.10°, and 0.25°. The squares of these bounds defined the variances for the random-number generator. Figure 7 shows the results of a single data run.

Thermal Expansion Port Misalignment Error

Figure 8 presents the effects of the thermal expansion on port misalignment. As mentioned earlier, the modeling of the thermal expansion of the leading edge is beyond the scope of this analysis, and only the deformation of the ramp surfaces was addressed. The reference temperature was assumed to be 70 °F and the skin thickness 0.5 in. The surface temperature was computed using the equilibrium oblique shock equations. A value of $4.4 \times 10^{-6}/°R$ was used for α_c, and a value of $7.562 \times 10^{-6}/°R$ was used for α_s. Computations were based on the distance from the nose—which is unconstrained and can move freely—to the pressure port.

Errors Caused by Transduction and Resolution

The transduction uncertainty and system resolution are important and must be carefully considered when developing a HY-FADS system. Depending on the needs of the measurement users, varying degrees of raw measurement quality and sampling resolution is required. For this analysis it was assumed that absolute pressure transducers were used. The analysis assumed a 40 lb/in² (5760 lb/ft²) full-scale reading for the three transducers connected to the ports nearest the stagnation point. A 15 lb/in² (2160 lb/ft²) full-scale reading edge was assumed for the rest of the transducers. Three transducer error levels were analyzed; these represent

1. Conventional sensors with 1-σ standard error at ± 0.5 percent of full scale

2. High-quality sensors with standard error at 1-σ ± 0.05 percent of full scale

3. State-of-the-art sensors with standard error of 1-σ ± 0.01 percent of full scale

Figure 9 shows the effects of the transduction error. The Mach-number error for the conventional sensors exceeds 0.96 at Mach 12; for the high-quality sensors the Mach-number error exceeds 0.36 at Mach 12. The

state-of-the-art sensors give a Mach-number error less than 0.06 at Mach 12.

Once the data were corrupted with measurement noise, they were sampled assuming 12-bit and 16-bit resolutions. Figure 10 presents the effects of the resolution errors. The Mach-number error induced by the 12-bit resolution is nearly 0.50 at Mach 12. The 16-bit resolution gives an error that is less than 0.05 at high Mach number. The effect on angle of attack is small for both resolution levels.

Collected Error Analysis: Monte-Carlo Simulation

Accuracy estimates for a state-of-the-art system were assessed. In this system all of the error models were incorporated. The system was assumed to have 16-bit resolution, and the transducers were assumed to have a noise level of less than 0.01 percent of full scale. The port layout was according to table 1 and the initial port layout uncertainty was assumed to have a 1-σ error of 0.05°. The sensor pneumatics used the configuration of table 2. To obtain ensemble averages of the errors induced by random input error components, the simulation was run repeatedly and model output statistics (MOSs) were generated. As such the simulation can be referred to as a Monte-Carlo simulation.

The 1-σ rms absolute error MOSs were listed for Mach number, dynamic pressure, altitude, angles of attack and sideslip, and as a function of free-stream Mach number in table 3. Presented also were the 1-σ rms percentage (of reading) error MOSs for Mach number, dynamic pressure, and altitude. As mentioned earlier, these results are contingent on the assumption that the aerodynamic models used are accurate.

Even at very high altitudes and Mach numbers at which the thermal conditions become the most extreme, the 1-σ measurement uncertainty still was less than 0.1 for at Mach 8, and less than 0.4 at Mach 12. The dynamic pressure measurement uncertainty was less than 5 lb/ft² for all of the Mach numbers analyzed.

Concluding Remarks

This paper addressed feasibility and uncertainty issues associated with applying a flush airdata sensing (FADS) system to the hypersonic flight experiment (HYFLITE) vehicle, which is a sharp-nose configuration of the type required for single-stage-to-orbit performance. Heating loads to be experienced by the HYFLITE make the use of intrusive airdata measurement devices impractical. Although the analysis in this paper was performed specifically for the HYFLITE vehicle, the methods described and the problems analyzed are considered generally applicable to hypersonic vehicles.

This study presented the physical layout of a candidate flush-port matrix, and the effects of various error sources on the overall system uncertainty were evaluated using an error simulation. In this simulation a realistic set of pressure data was generated along the trajectory and various error sources were superimposed on the data. The pressure data contaminated with the various error models were then used as input to an airdata estimation algorithm and effects resulting from the various error sources were analyzed by comparing the outputs of the estimation algorithm with the original trajectory data. Ensemble model output statistics were generated, and output error magnitudes resulting from the various (input) error sources were presented as a function of Mach number.

The error sources modeled include errors introduced by boundary-layer thickening caused by high-temperature viscous interactions, pneumatic lag induced by the pneumatic layout of the measurement sensors, and thermal transpiration resulting from high-temperature molecular creep in the pressure sensor pressure tubing. Other error sources modeled are misalignment errors in the initial pressure matrix layout, port misalignment errors resulting from thermal warping of the vehicle noseshape, sampling resolution error, and transducer sensing error. Nonequilibrium high-temperature gas effects and vehicle-dependent effects, such as bending about the center of gravity and position error, were not considered.

Simulation uncertainty estimates for a state-of-the-art system were presented. Even at very high altitudes and Mach numbers, at which the measurement conditions become the most extreme, the 1-σ measurement uncertainty still was less than 0.1 for Mach numbers up to 8, and less than 0.04 at Mach 12. The measurement uncertainty of dynamic pressure was less than 5 lb/ft^2 for all Mach numbers.

While the results presented are contingent on the assumption that the aerodynamic models used are accurate, a large range of potential error sources was modeled, and the results presented are believed to represent the types of accuracies that can be achieved by a hypersonic flush airdata sensing (HY-FADS) system. This report indicates that the HY-FADS measurement system is not only feasible for the HYFLITE vehicle, but that without extraordinary measures it is possible to obtain sufficiently accurate airdata results. The pressure measurements can be taken with very small diameter (0.01 in.) tubes to avoid problems with surface heating. A flush airdata system should be considered for future hypersonic test vehicles.

References

[1]Kock, Berwyn 1993: *HYFLITE III Concept Study Results*, NASP Paper No. 1275, presented at Monterey, CA, April 13.

[2]Gracey, William 1980: *Measurement of Aircraft Speed and Altitude*, NASA RP-1046.

[3]Siemers, P. M., III; Wolf, H.; and Henry, M. W. 1988: *Shuttle Entry Air Data System (SEADS)—Flight Verification of an Advanced Air Data System Concept*, AIAA Paper No. 88-2104.

[4]Larson, Terry J.; and Siemers, Paul M., III 1980: *Use of Nose Cap and Fuselage Pressure Orifices for Determination of Air Data for Space Shuttle Orbiter Below Supersonic Speeds*, NASA TP-1643.

[5]Larson, Terry J.; Whitmore, Stephen A.; Ehernberger, L. J.; Johnson, J. Blair; and Siemers, Paul M., III 1987: *Qualitative Evaluation of a Flush Air Data System at Transonic Speeds and High Angles of Attack*, NASA TP-2716.

[6]Whitmore, S. A.; Moes, T. R.; and Larson, T. J. 1992: *High Angle-of-Attack Flush Airdata Sensing System, J. Aircraft*, vol. 29, no. 5, Sept.–Oct., pp. 915–919.

[7]Whitmore, Stephen A.; and Moes, Timothy R. 1991: *The Effects of Pressure Sensor Acoustics on Airdata Derived From a High-Angle-of-Attack Flush Airdata Sensing (HI-FADS) System,* NASA TM-101736.

[8]Whitmore, Stephen A.; Moes, Timothy R.; and Leondes, Cornelius T. 1992: Development of a Pneumatic High-Angle-of-Attack Flush Airdata Sensing (HI-FADS) System. *Control and Dynamic Systems: Advances in Theory and Applications*, vol. 52, Academic Press, Inc., San Diego, pp. 453–511.

[9]Whitmore, Stephen A.; Moes, Timothy R. 1992: *Failure Detection and Fault Management Techniques for a Pneumatic High-Angle-of-Attack Flush Airdata Sensing (HI-FADS) System,* NASA TM-4335.

[10]Anderson, John D., Jr. 1989: *Hypersonic and High Temperature Gas Dynamics*, McGraw-Hill Book Co., New York.

[11]Hansen, C. Frederick 1959: *Approximations for the Thermodynamic and Transport Properties of High-Temperature Air*, NASA TR R-50.

[12]Huber, Paul W. 1963: *Hypersonic Shock-Heated Flow Parameters for Velocities to 46,000 Feet per Second and Altitudes to 323,000 Feet,* NASA TR R-163.

[13]Liepman, H. W.; and Roshko, A. 1978: *Elements of Gas Dynamics,* 3rd ed. John Wiley & Sons, Inc.

[14]Dongarra, J. J.; Bunch, J. R.; Moler, C. B.; Stewart, G. W 1979: *LINPACK User's Guide*. Siam Publishing, Philadelphia, PA.

[15]NOAA 1976: *U. S. Standard Atmosphere, 1976.* NOAA–S/T 76-1562, Washington, DC.

[16]Doebelin, Ernest O. 1983: *Measurement Systems, Application and Design,* 3rd ed. Mc-Graw Hill Book Co., New York.

[17]Avallone, Eugene A., ed.; and Baumeister, Theodore III, ed. 1984: *Marks' Standard Handbook for Mechanical Engineers*, *9th ed.* Mc-Graw Hill Book Co., New York.

[18]Kennard, Earle, H. 1938: *Kinetic Theory of Gases With an Introduction to Statistical Mechanics.* Mc-Graw Hill Book Co., Inc., New York.

REPORT DOCUMENTATION PAGE

1. AGENCY USE ONLY (Leave blank)	2. REPORT DATE June 1994	3. REPORT TYPE AND DATES COVERED Technical Memorandum

4. TITLE AND SUBTITLE

Measurement Uncertainty and Feasibility Study of a Flush Airdata System for a Hypersonic Flight Experiment

6. AUTHOR(S)

Stephen A. Whitmore and Timothy R. Moes

5. FUNDING NUMBERS

WU 505-68-40

7. PERFORMING ORGANIZATION NAME(S) AND ADDRESS(ES)

NASA Dryden Flight Research Center
P.O. Box 273
Edwards, California 93523-0273

8. PERFORMING ORGANIZATION REPORT NUMBER

H-2010

9. SPONSORING/MONOTORING AGENCY NAME(S) AND ADDRESS(ES)

National Aeronautics and Space Administration
Washington, DC 20546-0001

10. SPONSORING/MONITORING AGENCY REPORT NUMBER

NASA TM-4627

11. SUPPLEMENTARY NOTES

This memorandum originally appeared as AIAA-94-1930 and was prepared for the Applied Aerodynamics Conference, Colorado Springs, CO, June 20–23, 1994.

12a. DISTRIBUTION/AVAILABILITY STATEMENT

Unclassified—Unlimited
Subject Category 02

12b. DISTRIBUTION CODE

13. ABSTRACT (Maximum 200 words)

Presented is a feasibility and error analysis for a hypersonic flush airdata system on a hypersonic flight experiment (HYFLITE). HYFLITE heating loads make intrusive airdata measurement impractical. Although this analysis is specifically for the HYFLITE vehicle and trajectory, the problems analyzed are generally applicable to hypersonic vehicles. A layout of the flush-port matrix is shown. Surface pressures are related airdata parameters using a simple aerodynamic model. The model is linearized using small perturbations and inverted using nonlinear least-squares. Effects of various error sources on the overall uncertainty are evaluated using an error simulation. Error sources modeled include boundary-layer/viscous interactions, pneumatic lag, thermal transpiration in the sensor pressure tubing, misalignment in the matrix layout, thermal warping of the vehicle nose, sampling resolution, and transducer error. Using simulated pressure data for input to the estimation algorithm, effects caused by various error sources are analyzed by comparing estimator outputs with the original trajectory. To obtain ensemble averages the simulation is run repeatedly and output statistics are compiled. Output errors resulting from the various error sources are presented as a function of Mach number. Final uncertainties with all modeled error sources included are presented as a function of Mach number.

14. SUBJECT TERMS

Airdata; Hypersonic flight; Least-squares; NASP; Parameter estimation

15. NUMBER OF PAGES
19

16. PRICE CODE
AO3

17. SECURITY CLASSIFICATION OF REPORT	18. SECURITY CLASSIFICATION OF THIS PAGE	19. SECURITY CLASSIFICATION OF ABSTRACT	20. LIMITATION OF ABSTRACT
Unclassified	Unclassified	Unclassified	Unlimited